Draft version February 14, 2022
Preprint typeset using LaTeX style emulateapj v. 11/10/09

TWO LENSED LYMAN-α EMITTING GALAXIES AT z$\sim$5

Matthew B. Bayliss[1,2], Eva Wuyts[1,2], Keren Sharon[2], Michael D. Gladders[1,2], Joseph F. Hennawi[3], Benjamin P. Koester[1,2], Håkon Dahle[4]

Draft version February 14, 2022

ABSTRACT

We present observations of two strongly lensed $z \sim 5$ Lyman-α Emitting (LAE) galaxies that were discovered in the Sloan Giant Arcs Survey (SGAS). We identify the two sources as SGAS J091541+382655, at $z = 5.200$, and SGAS J134331+415455 at $z = 4.994$. We measure their AB magnitudes at $(i, z) = (23.34 \pm 0.09, 23.29 \pm 0.13)$ mags and $(i, z) = (23.78 \pm 0.18, 24.24^{+0.18}_{-0.16})$ mags, and the rest-frame equivalent widths of the Lyman-α emission at 25.3 ± 4.1Å and 135.6 ± 20.3Å for SGAS J091541+382655 and SGAS J134331+415455, respectively. Each source is strongly lensed by a massive galaxy cluster in the foreground, and the magnifications due to gravitational lensing are recovered from strong lens modeling of the foreground lensing potentials. We use the magnification to calculate the intrinsic, unlensed Lyman-α and UV continuum luminosities for both sources, as well as the implied star formation rates (SFR). We find SGAS J091541+382655 and SGAS J134341+415455 to be galaxies with $(\mathrm{L}_{Ly-\alpha},\ \mathrm{L}_{UV}) \leq (0.6\mathrm{L}^*_{Ly-\alpha}, 2\mathrm{L}^*_{UV})$ and $(\mathrm{L}_{Ly-\alpha},\ \mathrm{L}_{UV}) = (0.5\mathrm{L}^*_{Ly-\alpha}, 0.9\mathrm{L}^*_{UV})$, respectively. Comparison of the spectral energy distributions (SEDs) of both sources against stellar population models produces estimates of the mass in young stars in each galaxy: we report an upper limit of $\mathrm{M}_{stars} \leq 7.9^{+3.7}_{-2.5} \times 10^7\ \mathrm{M}_\odot h^{-1}_{0.7}$ for SGAS J091531+382655, and a range of viable masses for SGAS J134331+415455 of $2 \times 10^8\ \mathrm{M}_\odot h^{-1}_{0.7} < \mathrm{M}_{stars} < 6 \times 10^9\ \mathrm{M}_\odot h^{-1}_{0.7}$.

Subject headings: gravitational lensing:strong – galaxies: high-redshift galaxies

1. INTRODUCTION

Understanding the evolution of galaxies – especially the first generation of galaxies – remains one of the most important topics in astrophysics and cosmology. Populations of galaxies in the distant universe are identified over a wide range of wavelengths, including Distant Red Galaxies (DRGs), Ultra Luminous Infra-Red Galaxies (ULIRGs) and Sub-Millimieter Galaxies (SMGs). Many efforts to study the properties of high redshift galaxies at optical wavelengths focus on two distinct classes selected by their rest-frame UV properties: 1) Lyman-Break Galaxies (LBGs) and 2) Lyman-α Emitters (LAEs). LBGs are selected via deep wide-band photometry, identified by the 'Lyman limit' continuum break that appears at 912Å in the rest frame (Steidel et al. 1996a,b; Lowenthal et al. 1997) – though for sources at higher redshift this spectral break moves redward, approaching 1216Å in the rest frame due to the Lyman-α forest (Steidel & Sargent 1987; Rauch 1998) absorption by intergalactic neutral hydrogen. LAEs are selected by either narrow-band imaging (Cowie & Hu 1998; Rhoads et al. 2000, 2003; Ajiki et al. 2004; Gawiser et al. 2006; Yamada et al. 2005) or blind spectroscopy (Kurk et al. 2004; Sawicki et al. 2008) tuned to detect Lyman-α line emission redshifted into near-ultraviolet, optical, or near-infrared wavelengths. Over the past decade large samples of LBGs and LAEs have driven studies of star-forming galaxies at $z \gtrsim 2.5$.

Surveys for LBGs and LAEs are efficient for collecting statistical samples of high-redshift galaxies, but at $z \gtrsim 3$ they produce objects which are generally too faint to have their galactic continuum emission studied spectroscopically. The standard approach for studying the properties of these galaxy samples relies on stacking the photometric signal from many objects and fitting the observed mean SED against a variety of stellar population synthesis models in order to constrain parameters such as the ages and masses of the underlying stellar populations, as well as the amount of dust extinction (Shapley et al. 2003; Chary et al. 2005; Pirzkal et al. 2007; Lai et al. 2007; Finkelstein et al. 2008, 2009a; Nilsson et al. 2009; Yabe et al. 2009). In principal, stellar population synthesis modeling can also provide information about dust properties (i.e. the shape of the dust law) and metallicity, but even the stacked SED signal at $z \gtrsim 3$ is insufficient to constrain these additional parameters with much confidence. Broadly speaking, galaxies selected as LBGs are believed to sample more massive star-forming galaxies with an underlying older stellar population, and possibly higher dust content, while LAE selected galaxies

mbayliss@oddjob.uchicago.edu

[*] Based on observations obtained at the Gemini Observatory, which is operated by the Association of Universities for Research in Astronomy, Inc., under a cooperative agreement with the NSF on behalf of the Gemini partnership: the National Science Foundation (United States), the Science and Technology Facilities Council (United Kingdom), the National Research Council (Canada), CONICYT (Chile), the Australian Research Council (Australia), Ministério da Ciência e Tecnologia (Brazil) and Ministerio de Ciencia, Tecnología e Innovación Productiva (Argentina), and the Apache Point Observatory 3.5-meter telescope, which is owned and operated by the Astrophysical Research Consortium.

[1] Department of Astronomy & Astrophysics, University of Chicago, 5640 South Ellis Avenue, Chicago, IL 60637
[2] Kavli Institute for Cosmological Physics, University of Chicago, 5640 South Ellis Avenue, Chicago, IL 60637
[3] Max-Planck-Institut für Astronomie Königstuhl 17, D-69117, Heidelberg, Germany
[4] Institute of Theoretical Astrophysics, University of Oslo, P.O. Box 1029, Blindern, N-0315 Oslo, Norway

tend to be lower mass galaxies with low metallicities and very little dust (Giavalisco 2002; Venemans et al. 2005; Gawiser et al. 2007). Hubble Space Telescope imaging studies of high redshift LAE galaxies imply that these sources are compact, and likely either disk-like or irregular in structure (Pirzkal et al. 2007; Taniguchi et al. 2009). Recently Finkelstein et al. (2009c) modeled individual SEDs of 14 bright $z \sim 4.5$ LAEs from the Chandra Deep Field South and found a broad range in stellar population age, stellar mass, and dust extinction, which suggests that stacking SED analyses of high redshift galaxies may not be the best approach.

The main hurdle involved in studying any high redshift source is the general lack of signal. Distant galaxies are faint and therefore difficult to detect, and those which are identified are rarely – if ever – amenable to detailed follow-up. Furthermore, those sources which are bright enough to be studied individually are drawn from the extreme bright tail of the luminosity function of high redshift galaxies, and are therefore not necessarily representative of the bulk of the populations. In this paper we present two serendipitously discovered, strongly lensed high redshift galaxies: SGAS J091541+382655, spectroscopically confirmed at $z = 5.200 \pm 0.001$, with $r_{AB} = 24.68 \pm 0.25$, $i_{AB} = 22.92 \pm 0.09$ and $z_{AB} = 22.75 \pm 0.13$ mags, and SGAS J134330+415455 spectroscopically confirmed at $z = 4.994 \pm 0.001$, with $r_{AB} \geq 25.47$ mags, $i_{AB} = 23.36 \pm 0.18$ mags and $z_{AB} = 23.70^{+0.18}_{-0.16}$ mags. Both objects have riz colors and magnitudes that satisfy selection criteria for $r-$band dropouts in $z \sim 5$ dropout surveys, as well as Lyman-α equvialent widths (see Section 2) sufficiently large to be selected in surveys for Lyman-α excess. At $z \gtrsim 5$ these objects are the two brightest LAEs in the literature to date, and both sources are projected on the sky within $30''$ of the cores of confirmed strong lensing galaxy clusters. This means that the sources – once corrected for the lensing magnification – are intrinsically much fainter than the observed flux implies, and therefore provide a rare opportunity to study individual LAE properties at the fainter end of the luminosity function. There is a small but growing number of magnified galaxies at high redshift that are excellent candidates for high resolution spectroscopic follow-up (Koester et al. 2010; Wuyts et al. 2010); some of these galaxies have been observed in detail at optical and near-infrared wavelengths, including cB58 (Pettini et al. 2000), "the 8 O'clock Arc" (Allam et al. 2007; Finkelstein et al. 2009b), and "the Cosmic Eye" (Smail et al. 2007; Siana et al. 2009; Quider et al. 2010). The two galaxies discussed in this paper are the first $z \sim 5$ galaxies that present similar opportunities for detailed study via follow-up spectroscopy.

Where necessary we calculate cosmological distances assuming a flat cosmology with $H_0 = 70$ km s^{-1} Mpc^{-1}, and matter density $\Omega_M = 0.3$. All magnitudes are AB.

2. OBSERVATIONS

2.1. *Data*

The two sources presented here were first identified as r-band dropouts in gri imaging of two different strong lensing galaxy clusters, and subsequently confirmed by spectroscopy to have strong Lyman-α emission features. The two galaxy clusters were identified as part of the Sloan Giant Arcs Survey (SGAS; Hennawi et al. 2008), a blind survey for strong lensing systems in optically selected massive clusters at $0.1 \leq z \leq 0.6$ detected via the Red-Sequence Cluster algorithm (Gladders & Yee 2000) adapted to run on the Sloan Digital Sky Survey (SDSS; York et al. 2000) public data release catalogs. Strong lensing clusters are identified by visual inspection of imaging in $g-$band on 2m to 4m-class telescopes for 600s in $< 1''$ seeing, and the most spectacular systems have been followed-up with multi-band imaging and spectroscopy on 8m-class telescopes. One of the clusters discussed here, SDSS J1343+4155, appears in a recent small sample of strong lensing clusters discovered in the SDSS by Diehl et al. (2009). The other cluster, SDSS J0915+3826, does not appear in any prior published work. Imaging and spectroscopic observations were conducted with the Frederick C. Gillett Telescope (Gemini North) between the months of 2008 February and 2008 July. The GMOS imaging observations were pre-imaging conducted for the purpose of spectroscopic mask design. Both imaging and spectroscopy were part of Gemini program GN-2008A-Q-25. The primary goal of the spectroscopic observations was to obtain redshifts of arcs to facilitate strong lensing modeling. We briefly summarize the spectroscopy here, and refer the reader to Bayliss et al. (2010), in preparation, for additional details.

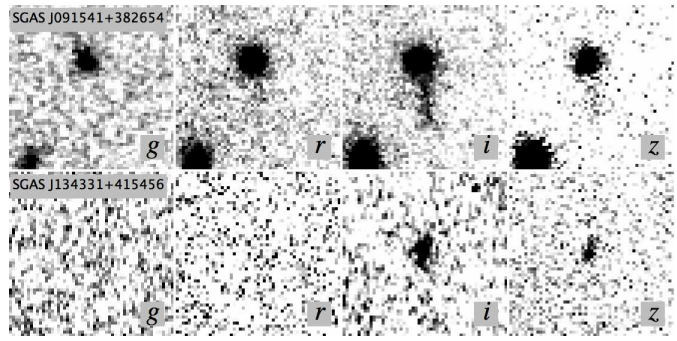

FIG. 1.— GMOS $griz$ (from left to right) $8'' \times 8''$ cutout images centered on SGAS J091541+386254 and SGAS J134331+415455. Both objects exhibit obvious drop-out behavior from the $i-$ to $r-$bands. The $z-$band detection of SGAS J091541+386254 appears at lower significance than its counterpart for SGAS J134331+415455 because its z data were taken during bright time and the sky background noise is $\sim 30\%$ higher.

Gemini North/GMOS gri photometry for both cluster fields are derived from 2x150s dithered exposures, which were executed in queue mode on February and March of 2008. These pre-imaging data were used for spectroscopic mask design and target prioritization. GMOS z-band observations consisted of 6x180s dithered exposures which were scheduled as follow-up, primarily in order to measure the continuum flux of the LAEs, and were executed in queue mode in February of 2010. The GMOS images were reduced using the Gemini IRAF[6] package.

In addition to the GMOS-N photometry and spectroscopy, we obtained near-infrared (NIR) imaging of the two lensing clusters in the *z'JH* filters with the Near-Infrared Camera and Fabry-Perot Spectrometer (NIC-FPS) of the 3.5m telescope at the Apache Point Obser-

[6] IRAF (Image Reduction and Analysis Facility) is distributed by the National Optical Astronomy Observatories, which are operated by AURA, Inc., under cooperative agreement with the National Science Foundation.

vatory (APO) in New Mexico. The detector is a Rockwell Hawaii 1-RG 1024x1024 HgCdTe device with a pixel scale of $0.273''$ pixel^{-1} and a 4.58×4.58 arcmin unvignetted field of view. The APO/NIC-FPS z' data differs from the Gemini/GMOS z significantly due to the different wavelength responses of the NIC-FPS and GMOS detectors. The effective wavelengths of the two filters are offset by $\sim$ 1000Å, and we use the prime ($'$) throughout this paper to distinguish the APO/NIC-FPS z' from the Gemini/GMOS z. The NIR data were taken on 3 different nights in the Winter and Spring of 2009. The conditions during the observing nights varied, with subarcsecond seeing for the SDSS J1343+4155 *z'*-band and both *J*-band images. The SDSS J0915+3826 *z'*-band and both *H*-band images were taken in $\sim 2''$ seeing. The observations consisted of 5-point dithers around a $40''$ box and were reduced, registered and stacked using a custom IRAF pipeline. Total exposure times are 5400s, 6960s and 3500s for *z'*-, *J*-, and *H*-band observations of SDSS J0915+3826 and 7800s, 5160s and 2625s for *z'*-, *J*-, and *H*-band observations of SDSS J1343+4155.

The SDSS was used to calibrate the four optical bands and the Two Micron All Sky Survey (2MASS) was used to calibrate the NIR observations. Prior to making any photometric measurements we first transform images in all bands to the reference frame of the *i*-band image, $0.1454''$ pixel^{-1} (GMOS-North detector, binned 2x2). We then construct an empirical, normalized point spread function (PSF) for each image based on a well-defined, non-saturated reference star. We create photometric apertures by drawing a ridge line that covers the high-redshift LAE and convolving it with the appropriate PSF for each image. Apertures are defined by an equivalent radius, which corresponds to the radius of a circular aperture that goes out to the same isophot. We make the final magnitude measurement using a detailed sequence of sky subtraction and outlier masking steps; first we subtract a general sky measurement and then compute the median pixel value and standard deviation inside annuli of fixed width at increasing radial distances from the source. Far enough out, these median values converge to zero for an accurate sky subtraction. We average the median values at large radii and subtract this average from the image to correct the general sky subtraction. Outliers are defined as pixel values that deviate by more than 5σ from the median in the respective annuli, and are replaced by the median value plus an appropriate noise term. The final magnitude is measured at an equivalent radius of twice the FWHM of the PSF and corrected to an equivalent radius of $6''$ based on the curve of growth of the PSF. By defining the radius as twice the FWHM, we make sure our apertures always cover the same physical region on the sky. In the case of SGAS J091541+382655, a foreground galaxy lies very close to and partially on top of the LAE galaxy. We use the `GALFIT` package (Peng et al. 2002) to fit a Sersic profile to this galaxy in the imaging data where the LAE has no measureable flux, and then scale the galaxy model by the peak flux in each band and subtract it out before measuring the LAE magnitudes.

When the LAEs are not detected (in gJH for SGAS J091541+382655 and $grJH$ for SGAS J134331+415455), we measure a limiting magnitude, derived from the total sky noise in the aperture. We define a sky noise per pixel σ_{sky} as the standard deviation of our overall sky measurement plus a contribution from the poison error made in this measurement. A pixel value of $2\sigma_{sky}$ is added in quadrature for each pixel in our final aperture with an equivalent radius equal to twice the FWHM. The limiting magnitudes are also aperture corrected to an equivalent radius of $6''$. This method constrains the source to be fainter than the limiting magnitudes at 95% confidence in the relevant bandpasses.

All spectroscopic observations were carried out using the Gemini Multi-Object Spectrograph (Hook et al. 2004) using custom slitmasks that were designed to target lensed sources based on their color, morphology, and positoin in the GMOS imaging. After targeting all of the arc candidates, any remaining slits were placed on cluster members, easily identified by their red sequence colors. Spectra were taken using the macroscopic nod-and-shuffle (N&S) mode available on GMOS. The reasons for using N&S are threefold. First, many of the emission or absorption features that are used to determine galaxy redshifts in the range $z = 1.0 - 3.0$ characteristic of the giant arcs, are in the redder part of the optical where sky lines are problematic, and N&S facilitates more accurate sky-subtraction (Glazebrook & Bland-Hawthorn 2001), particularly at low spectral resolution. Second, N&S sky-subtraction allows us to use very small $1'' \times 1''$ microslits that can be densely packed into the cluster core ($\sim 30''$), allowing us to target as many arcs, arclets, and cluster galaxies as possible (Gilbank et al. 2008) . Third, as we are primarily interested in a number of objects around the cluster center, the density of objects and the limited field of interest are perfect for block-shuffling N&S observations. Spectra were taken with the R150_G5306 grating in first order which gives a dispersion of 3.5Å per pixel (binned spectrally by two), with six pixels per resolution element resulting in a spectral FWHM $\simeq$ 940 km s^{-1}. Although the R150 grating offers broad spectral range from the atmospheric cutoff to $\lambda \gtrsim 1\mu$m, the drop in sensitivity at the blue and red extremes, due both to the GMOS CCD and the R150 grating efficiency, results in effective spectral coverage of $\sim 4000 - 9500$Å .

The N&S technique employed in our program is non-standard in that it involves a nod distance on the sky that is half the size of the macroscopic shuffle. The mask is designed to incorporate two submasks, each of which is a set of slits covering an area one third the size of the detector. Slits for the two submasks overlap on the sky in an area that is one sixth the size of the detector (because the nod distance is set to half the shuffle distance). This design allows us to place science slits for the primary target – the core of a strong lensing cluster in this case – on both submasks and obtain useful spectra for the entire duration of the N&S exposure, whereas standard macroscopic N&S results in science spectra for only half of the total exposure time. Our integration times were 2400s resulting in a 1200s effective integration for each of the two submasks. Two exposures were taken for each target. Thus if an arc was targeted on both submasks (typical for the most prominent arcs) the total integration time was 4800s. N&S facilitates straightforward sky subtraction by differencing two sections of the detector

– each 1/3 the size of the full detector. The spectra presented here were wavelength calibrated, stacked, extracted and analyzed using a custom pipeline based on the XIDL software package[7].

2.2. *SGAS J091541+382655*

SDSS J0915+3826 is a new strong lensing cluster that was discovered in the SGAS – discussed above. We measure redshifts for 16 cluster members in our Gemini/GMOS spectroscopy and combine this new data with a redshift for the BCG measured in the SDSS to identify a mean cluster redshift of $z = 0.397$ and a velocity dispersion of 870 ± 169 km s^{-1}. The most prominent strong lensing feature around this cluster is a bright blue arc that we identify as a background galaxy at $z = 1.501$ from O[II]λ3727Å, CII]λ2328Å, CIII]λ1907, 1909Å in emission, as well as AIIIλ1855, 1863Å in absorption. Pre-imaging of this cluster reveals a source near the cluster core that exhibits a dramatic drop in flux from the i- to r-band, as shown in Figure 1. With Gemini/GMOS-N, in *griz*, we measure this source at $g_{AB} \geq 26.07$, $r_{AB} = 24.86 \pm 0.25$, $i_{AB} = 23.34 \pm 0.09$, and $z_{AB} = 23.29 \pm 0.13$. Slits were placed on this source in both submasks for our N&S observation of this cluster and the spectra exhibit bright emission at 7539Å which we interpret as Lyman-α λ1216Å at $z = 5.200$.

The LAE galaxy in this case is located on the sky very near to a foreground galaxy, and so we took care to account for possible contamination in the LAE spectrum by light from the galaxy that falls into the slit, as this could mimic a continuum break in the source spectrum. The separation between the LAE box slit and the potentially contaminating foreground galaxy is 2.5″. Examination of the radial profile of the potential contaminant in the pre-imaging observation shows that the i-band flux within the LAE slit due to the galaxy is on average 1.5×10^{-3} of the peak flux of that galaxy. The mean i-band flux of the LAE within the spectroscopic aperture is 5.1×10^{-2} compared to the peak of the contaminating galaxy, and thus assuming comparable seeing between the imaging and spectroscopic observations suggests that this object's contribution to the i-band flux within the LAE aperture is approximately 3% of the total light. Note that given the separation between the contaminant and the slit the seeing of the spectroscopic and imaging observations would have to be grossly different to produce significant contamination; such a mismatch is neither expected due to execution of the observations in specified conditions in queue mode, nor suggested by the spatial width of stellar spectra within the alignment boxes of the spectroscopic observations.

The relevant part of the extracted spectrum is displayed in Figure 2, and despite the low dispersion grating used for our observations the line is measurably asymmetric. We also detect continuum signal redward of the emission line and no significant signal blueward of it. This source has a strong photometric r-i break – even after subtracting the emission line flux from the i-band photometry. It is also very blue in i-z, and is not detected in NIC-FIPS imaging to a 2-σ limiting magnitude of $J_{AB} \geq 22.49$, indicatingg that the continuum spectral slope redward of the emission feature is blue. The blue continuum redward of the emission and the strong r-i break – along with the non-detection in g, and the asymmetry of the line confirm the interpretation of the source as a Lyman-α emitting galaxy at high redshift. The most likely candidate emission lines which confuse searches for high-redshift LAEs are O[II]λ3727Å, [OIII] λ5007Å and H-α, but for each of these other candidate lines we would expect accompanying emission features to fall within the wavelength coverage of our spectroscopy. We measure the equivalent width of the Lyman-α emission by fitting a simple power-law to the continuum spectrum redward of the emission line over a wavelength range of $7575 - 8275$Å, and subtracting the underlying continuum flux from the emission line. Over the relatively small wavelength range used the continuum level is consistent with a constant value. We note that our spectral flux calibration uses a standard from the Gemini archive to correct roughly for the detector sensitivity as a function of wavelength, but is not suitable for measuring absolute fluxes from the spectral data. Taking into account the underlying continuum and the source redshift we measure a rest-frame EW for the Lyman-α emission of 25 ± 4Å, and combine the EW measurement with our $i-$band photometry to calculate an observed Lyman-α line flux of $2.1 \pm 0.7 \times 10^{-16}$ ergs s^{-1} cm^{-2}.

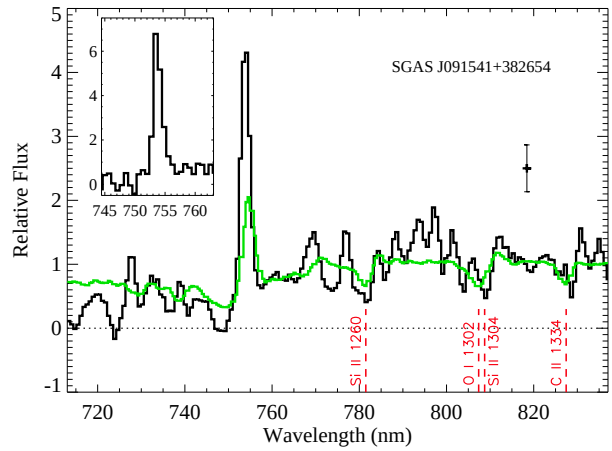

FIG. 2.— GMOS spectrum of the Lyman-α emitter behind cluster lens SDSS J0915+3826. The LAE spectrum plotted over a range of $\sim 7150 - 8350$Å is smoothed to a scale comparable to a the spectral resolution of 940 kms^{-1} in order to emphasize the low-significance candidate absorption features, with the composite Lyman Break Galaxy absorption+emission spectrum from Shapley et al. (2003) overplotted in green. Dashed vertical lines indicate the location of prominent UV continuum metal absorption lines at the LAE redshift, which coincide with the low-significance features in our continuum spectrum. The Lyman-α emission feature is also shown inset, without smoothing. A typical spectral flux error bar is displayed on the right side of the figure, in the whitespace above the continuum.

2.3. *SGAS J134331+415455*

The second lensed LAE presented here is located near the strong lensing cluster SDSS J1343+4155, which was previously identified as a strong lensing cluster in the SDSS by Wen et al. (2009) and Diehl et al. (2009). We combine our Gemini/GMOS spectroscopy with two cluster member redshifts from the SDSS to measure a mean cluster redshift of $z = 0.418$ and a velocity dispersion of 1077 ± 266 km s^{-1} from 7 cluster member galax-

[7] http://www.ucolick.org/~xavier/IDL/index.html

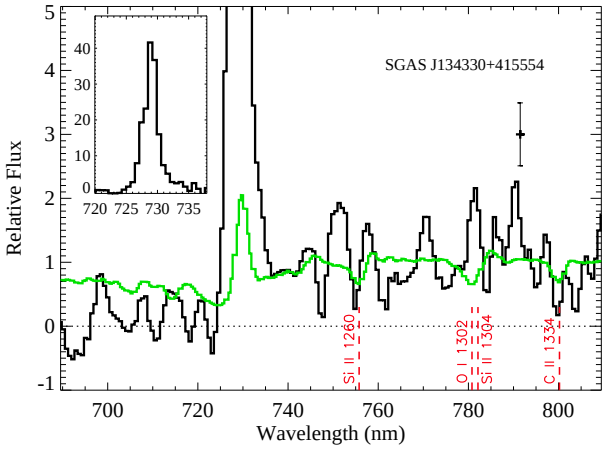

FIG. 3.— GMOS spectrum of the Lyman-α emitter behind cluster lens SDSSJ1343+4155. The spectrum is presented identically to the spectrum shown in Figure 2, except that it covers an observer-frame wavelength range of $\sim 6900 - 8100$Å.

ies. The bright arc around this lens is spectroscopically identified by Diehl et al. (2009) as a background galaxy at z= 2.091. Pre-imaging of this cluster reveals a source near the cluster core that exhibits a dramatic drop in flux from the i- to r-band – shown in Figure 1. We measure this source at $g_{AB} \geq 25.97$, $r_{AB} \geq 25.64$, $i_{AB} = 23.78 \pm 0.12$, and $z_{AB} = 24.24^{+0.18}_{-0.16}$. We placed slits on this source in each of the two submasks for our spectroscopic N&S observations of this cluster. The spectra corresponding to these slits exhibit a bright emission line at 7289Å, which we interpret as Lyman-α λ1216Å at $z = 4.994$.

The extracted spectrum around the emission feature is displayed in Figure 3. The emission feature is significantly asymmetric and we measure continuum emission redward of the line, but no continuum blueward. The source is undetected in NIC-FIPS imaging down to a 2-σ limiting magnitude of $J_{AB} \geq 22.22$. Similarly to the case of SGAS J091541+382655, this source has a blue i-z color and our NIR photometry implies that it has a blue continuum spectral slope redward of the emission feature. The most likely candidate emission line which could be misinterpreted as Lyman-α in this spectrum is O[II] λ3727Å, but we rule this out as a realistic interpretation based on the absence of H-β λ4862Å and O[III] λ4960, 5007Å, both of which should fall just within the spectral range covered by our data if the source were a very red galaxy at lower redshift. Other common contaminants in searches for high-redshift LAEs include [OIII] λ5007Å and H-α, but in each of these cases we would also expect to observe other accompanying emission features given the wavelength coverage of our spectroscopy. We measure the equivalent width of the Lyman-α emission by fitting a simple power-law to the continuum spectrum redward of the emission line over a wavelength range of $7400 - 8275$Å, and subtracting the underlying continuum flux from the integrated flux from the emission line. Similar to the continuum fit for SGAS J091541+382655, the continuum level for SGAS J134331+415455 is consistent with a constant value. Taking into account the continuum and the source redshift we measure a rest-frame EW for the Lyman-α emission of 136 ± 20Å and an combine the EW measurement with our $i-$band photometry to calculate an observed Lyman-α line flux of $2.1 \pm 0.5 \times 10^{-16}$ ergs s^{-1} cm^{-2}.

3. ANALYSIS

3.1. *Lens Models and Intrinsic Source Properties*

Using the measured equivalent widths and i magnitudes we also calculate lensed isotropic Lyman-α line luminosities of $L_{Ly-\alpha} = 5.9 \pm 1.1 \times 10^{43}$ erg s$^{-1}h^2_{0.7}$ and $L_{Ly-\alpha} = 5.4 \pm 0.9 \times 10^{43}$ erg s$^{-1}h^2_{0.7}$ for SGAS J091541+382655 and SGAS J134331+415455, respectively. These are not the true isotropic luminosities because both sources are lensed by foreground galaxy clusters, and are therefore significantly magnified. To measure the intrinsic luminosities of the LAEs, we estimate the magnification due to strong lensing by the intervening clusters. The mass models are constructed using the publically available software, `LENSTOOL` (Jullo et al. 2007), with Monte Carolo Markov Chain (MCMC) minimization in the source plane, and are shown in Figure 4. For SDSS J1343+4155, we compute a simple mass model using as constraints the giant blue arc at $z = 2.09$, the LAE at $z = 4.994$, paired with a counter image candidate that we have identified. The cluster and the brightest cluster galaxy (BCG) are represented by pseudo isothermal elliptical mass distributions (PIEMD; Jullo et al. 2007). We allow all the parameters of the cluster halo to vary. For the BCG, we follow the light distribution for the positional parameters, and vary the core and cut radii and the velocity dispersion. Our best-fit model reproduces the locations and orientations of the observed lensed images, and is consistent with the measured velocity dispersion to within the uncertainty. Based on this model, the magnification at the location of the LAE is $m \sim 12$, which we use to calculate the intrinsic isotropic Lyman-α line luminosity for SGAS J134331+415455 to be $L_{Ly-\alpha} = 4.5 \pm 0.7 \times 10^{42}$ erg s$^{-1}h^2_{0.7}$. Assuming Case B recombination and taking the prescription from Kennicutt (1998) we calculate the star-formation rate (SFR) for SGAS J134331+415455 to be $SFR_{Ly-\alpha} = 4.1 \pm 0.6$ M$_\odot$ yr$^{-1}h^{-1}_{0.7}$. Applying a mangification correction to the apparent magnitude in $z-$band we find the intrinsic $z-$band AB magnitude to be $z = 27$. We can also estimate the SFR from the UV continuum flux density at 1500Å according to equation (1) from Kennicutt (1998), which results in $SFR_{UV} = 18 \pm 3$ M$_\odot$ yr$^{-1}h^{-1}_{0.7}$.

The strong lensing model for SDSS J0915+3826 is constrained by the positions of the components of the giant arc. We do not identify a clear counter image for the LAE, and therefore do not use it as a constraint. We represent the lens with a single PIEMD and allow all its parameters to vary, which produces a velocity dispersion estimate that is similar to the value we measure from spectroscopy of cluster members (see Section 2.2). The critical curves for our best-fit model are plotted in Figure 5. Since the available constraints are internal to the radial projection of the LAE, the predicted LAE magnification is highly uncertain. In particular, if we compute a set of models with parameters in the range allowed by the uncertainties, the location of the critical curve for

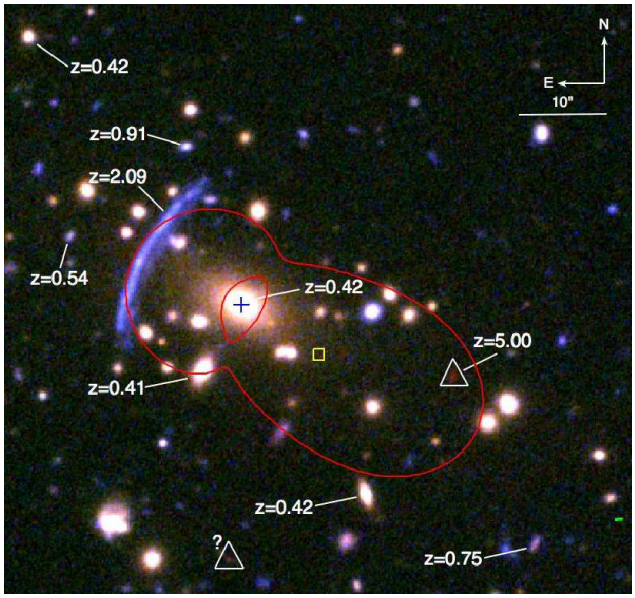

FIG. 4.— The field of SDSS J1343+4155 with tangential and radial critical curves for the bright main arc overplotted. One image of the lensed background LAE, spectroscopically confirmed at $z = 4.994$, and its putative counterimage predicted by the lensing model are identified by white triangles. The center of the dark matter halo and BCG mass components are indicated by a square and cross, respectively. Other sources in the field – background objects and cluster members – are labeled with their spectroscopic redshifts. Color images are created from Gemini+GMOS-North *gri* 300s pre-imaging data.

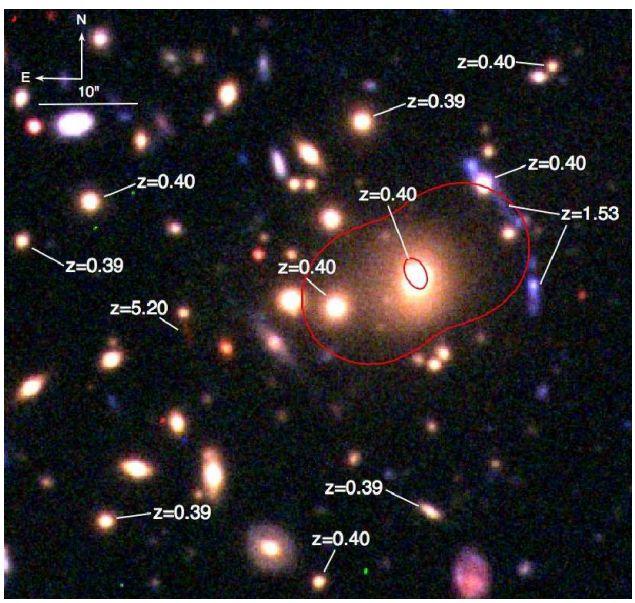

FIG. 5.— The field of SDSS J0915+3826 with the tangential critical curve for the bright main arc overplotted. Other sources with spectroscopic redshifts are also identified, including the lensed background LAE at $z = 5.200$. Color images are created from Gemini+GMOS-North *gri* 300s pre-imaging data.

the LAE varies significantly and there is practically no upper limit for the implied magnification. Since in all cases the magnification is higher than ~ 10, we adopt this number as our working order-of-magnitude estimate and determine an upper limit for the intrinsic isotropic Lyman-α line luminosity for SGAS J091541+382655 of $L_{Ly-\alpha} \leq 5.9 \pm 1.1 \times 10^{42}$ ergs s$^{-1}h_{0.7}^{2}$ and a corresponding $SFR_{Ly-\alpha} \leq 5.3 \pm 1.0$ M$_\odot$ yr$^{-1}h_{0.7}^{-1}$. Correcting the $z-$band magnitude for the lensing mangifciation we recover an intrinsic magnitude of $z \geq 25.75$ mags, from which we measure $SFR_{UV} \leq 51 \pm 7$ M$_\odot$ yr$^{-1}h_{0.7}^{-1}$ using equation (1) from Kennicutt (1998).

We note that $SFR_{Ly-\alpha}$ and SFR_{UV} differ significantly for both sources. For SGAS J134331+415455 $SFR_{Ly-\alpha}$ is lower than SFR_{UV} by a factor of 4.5, which is consistent with previous studies finding that the SFR calculated from Lyman-α emission is often systematically lower than other SFR metrics – such as UV continuum flux density at 1500Å – by a factor of ~ 5 or more (Tapken et al. 2007). The disagreement between the two SFR estimates is more extreme for SGAS J091541+382655, with $SFR_{UV} \sim 9\times$ larger than $SFR_{Ly-\alpha}$. In a study of LAEs at $z = 3.1$ identified in the Chandra Deep Field South, Gronwall et al. (2007) find on average, $SFR_{UV}/SFR_{Ly-\alpha} \sim 3$ with a large scatter about the mean, including several objects with $SFR_{UV}/SFR_{Ly-\alpha}$ as large as we measure for SGAS J091541+382655. Significant differences between these two SFR calibrations are understandable considering the potential systematic errors involved in measuring the SFR from both UV continuum and Lyman-α emission. For example, resonant scattering of Lyman-α photons off of neutral hydrogen can supress observed Lyman-α emission if there is even a very small amount of dust in the source galaxy, thus producing an underestimate of $SFR_{Ly-\alpha}$. Additionally, Kennicutt (1998) identifies several caveats associated with the SFR_{UV} calibration, including assumptions about the IMF and the timescale and manner of star-formation (e.g. constant vs. burst). Specifically, equation 1 in Kennicutt (1998) recovers SFR from the rest-frame UV flux by assuming a galaxy has undergone continuous star formation for 10^8 years or longer, and originates from a Salpeter IMF with mass limits of 0.1 and 10 M$_\odot$. If the properties of the underlying stellar populations in either of these galaxies differ significantly from the parameters assumed in Equ. 1 from Kennicutt (1998) then there will be systematic differences between the SRFs estimated from the rest-frame UV flux and the true SFRs.

We have also considered the possibility that the Lyman-α emission in one or both of these objects could be due all or in part to AGN activity. Given the lack of detection of significant emission from highly ionized species, such as N[V] and C[IV], we conclude that it is unlikely that AGN are playing a significant role in the observed Lyman-α emission. The disagreements between the two SFR estimates for the two sources discussed here highlight the difficulty in making robust SFR measurements from source-frame UV observables.

Having accounted for the magnification due to gravitational lensing, we can also compare the luminosities of these two sources to large samples of LAEs and LBGs at comparable redshifts (Hu et al. 2004; Shimasaku et al. 2006; Bouwens et al. 2007; Dawson et al. 2007; Murayama et al. 2007; Ouchi et al. 2008; McLure et al. 2009, e.g.,). Studies of luminosity functions at high redshift are challenging, and parameters such as L* and α are not nearly so well measured as they are in the nearby universe. For comparing Lyman-α luminosities, we take the average of 6 different measurements of $L^*_{Ly-\alpha}$ values from Ouchi et al. (2008) that were

fit using samples of LAEs at $z \sim 3.7$ and $z \sim 5.7$, assuming three possible values of the faint end slope of the luminosity function, α. For the purpose of comparing continuum luminosities, we take L^*_{UV} as the average of the two L^*_{1500} best-fit values for LAEs at $z \sim 3.7$ and $z \sim 5.7$ from Ouchi et al. (2008). SGAS J091541+382655 is ($L^*_{Ly-\alpha}$, L^*_{UV}) $\leq$ ($0.6L^*_{Ly-\alpha}$, $2L^*_{UV}$), and SGAS J134331+415455 is ($L^*_{Ly-\alpha}$, L^*_{UV}) = ($0.5L^*_{Ly-\alpha}$, $0.9L^*_{UV}$). Both of these galaxies live at $\lesssim L^*$ on the luminosity function for similar galaxies at comparable redshifts, which makes them interesting targets for studying the properties of typical LAEs at $z \sim 5$ on an individual basis.

We also attempt to measure the morphologies of both lensed LAEs in our Gemini/GMOS imaging and place constraints on the intrinsic sizes of these two galaxies. Neither source is detected at $S/N \gtrsim 12$, which limits our ability to make detailed morophological measurements or shape fits, but we can check the object profiles against the image PSFs and use our estimates of the magnification due to lensing to place some rough constraints on the physical sizes of these galaxies. Studies of LAE morphologies at $z = 3.1$ using HST imaging find that the Lyman-α and restframe UV emission from these sources are spacially coincident and have half-light radii $\lesssim$ 1.5kpc (Bond et al. 2009, 2010). Bond et al. (2009) argue that S/N$\gtrsim$ 30 is necessary to make robust measurements of half-light radii for LAEs, and find that it is difficult to distinguish between resolved and unresolved compact cores at S/N$\lesssim$ 30. The two lensed LAEs are best-detected in our Gemini/GMOS $i-$band imaging, so this is the data we use for our morphological measurements.

SGAS J134331+315455 is slightly elongated in the tangential direction with respect to the center of the cluster. We measure its profile to be consistent with a gaussian along the tangential axis with a FWHM= $1.1''$, and consistent with a gaussian of FWHM= $0.57''$ along the radial axis. The FWHM of the PSF measured from stars in the image is $\sim 0.57''$, suggesting that the LAE is unresolved along one axis and resolved along the other. This kind of morphology is natural for a strongly lensed background source where the magnification is generally much greater along one axis that the other; a source located on the tangential caustic will be highly magnified in the tangential direction with respect to the center of the lensing potential, and magnified very little or not at all in the radial direction. We conclude that SGAS J134331+415455 is unresolved in the radial direction and barely resolved in the tangential direction. Assuming that all of the magnification factor of $m = 12$ is applied in the tangential direction, we convert a FWHM of $1.1''$ into a physical linear size of $\sim$ 0.6kpc, which indicates that most of the emission from this galaxy originates from a region very compact in size. This constraint must be taken with the caveat that the data are lower S/N than would be optimal, but the signficant linear magnification of these sources due to gravitational lensing does enable us to probe very physically interesting scales even with ground-based imaging. We also measure the locations of SGAS J134331+415455 to be identical in the Gemini/GMOS $i-$ and $z-$band images to the accuracy of our astrometry, $\sim$ 0.2", corresponding to physical scales of $\sim 100pc$. Based on the observer frame equivalent width

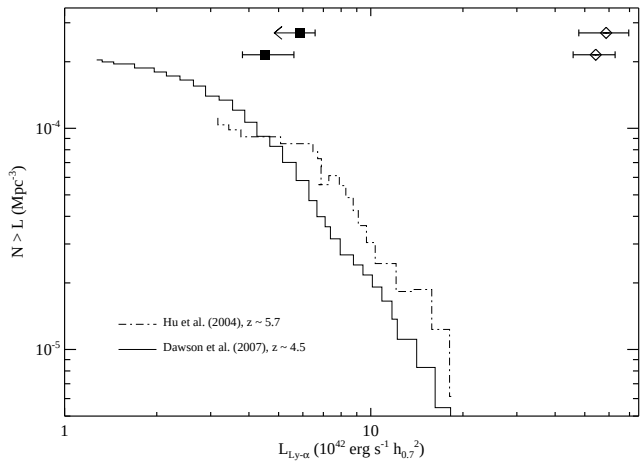

FIG. 6.— Two empirical cumulative Lyman-α line emission luminosity functions (uncorrected for completeness) for LAEs at high redshift are plotted; a sample of $z \sim 4.5$ LAEs published by Dawson et al.(2007) is given by the solid histogram and a sample of $z \sim 5.7$ LAEs (Hu et al. 2004) by the dot-dashed histogram. Both the apparent (magnified) and intrinsic Lyman-α luminosities for the two sources presented in this paper. Open diamonds indicate the apparent luminosities and filled squares indicate the intrinsic luminosities, corrected for the magnification (where we have only an upper limit to the intrinsic luminosity for SGAS 091541+382655). The magnification due to strong lensing allows us to probe deep down the Lyman-α luminosity function with sources that are observationally the brightest two LAEs known at $z \sim 5$.

of this source, the flux in the $i-$band filter is $\sim$ 60% Lyman-α line emission, whereas the $z-$band filter measures only rest-frame UV continuum emission. Given the spatial coincidence of the LAE in the $i-$ and $z-$bands we conclude that the UV continuum and Lyman-α emission cannot originate from regions separated by more than of order $\sim 100pc$ projected onto the sky. We have no measurement of the relative velocities of the UV continuum and the Lyman-α emission and therefore cannot constrain a possible separation in velocity.

SGAS J091541+382655 is similar to SGAS J134331+415455 in that the LAE is elongated on the tangential axis relative to the center of the lensing cluster. Using the `GALFIT` subtracted $i-$band image, we measure the LAE to be resolved in the tangential direction, having a shape consistent with a gaussian of FWHM= 1.82", which equates to a constraint on the physical scale of $\leq$ 1.2kpc, where the lower limit on the magnification of this source translates to an upper limit in the physical size (and again assuming that the magnification is entirely along the tangential diretion). We also measure the LAE to have a gaussian shape with $FWHM = 0.75''$ in the radial direction, which – given the FWHM$\sim 0.73''$ measured from the PSFs of stars in the image – is consistent with the source being unresolved in the radial direction. In the observer frame the equivalent width of the Lyman-α emission for this source is $EW_{Ly-\alpha} = 157$Å, from which we estimate that Lyman-α photons are contributing less than 20% of the $i-$band flux, so that we cannot make any attempt to measure a spatial offset between the Lyman-α and UV continuum emission. Our size constraints for both sources are in good agreement with the literature, in that we find the sizes of the LAEs to be consistent with compact sources of size $\lesssim$ 1.5kpc.

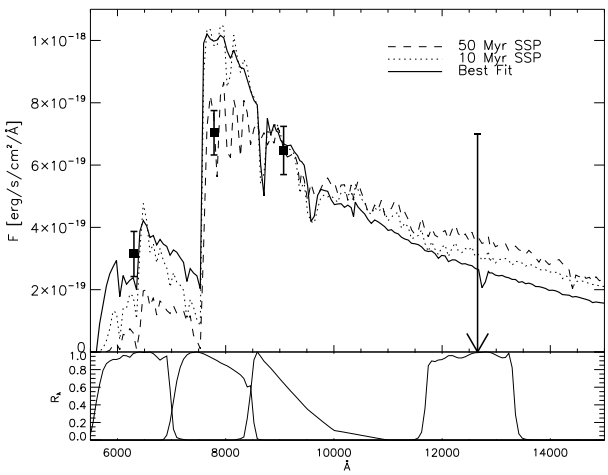

FIG. 7.— The best-fit spectral energy distribution for SGAS J091541+382655 is plotted with a solid line on top of the photometric data. The dotted and dashed lines are dust-free, single burst models from CB07, with ages of 10 Myr and 50 Myr respectively, scaled to match the observed z-band flux. This illustrates that the photometry favors a young (i.e. blue) stellar population, the 50 Myr model already deviates considerably from the best-fit SED. Filter transmission curves corresponding to the r, i, z and J photometry are plotted in the bottom panel.

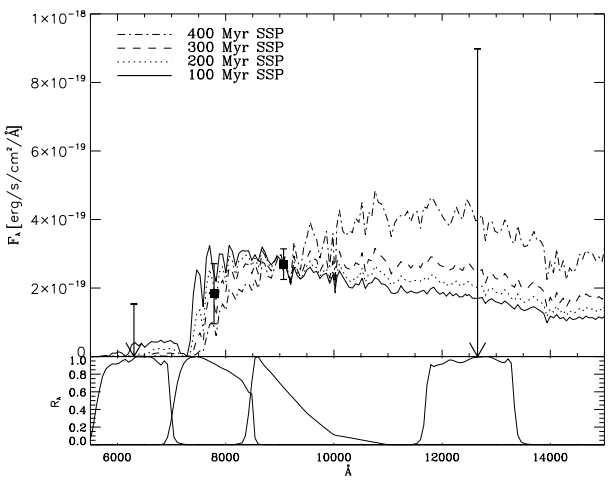

FIG. 8.— Dust-free single burst CB07 models are scaled to match the z-band flux and plotted on top of the photometric data for SGAS J134331+415455. Models with ages anywhere in the range of 100 Myr to 400 Myr are potentially good fits for the limited data in-hand. Filter transmission curves corresponding to the r, i, z and J photometry are plotted in the bottom panel.

3.2. *Stellar Mass and UV Continuum Properties*

With several photmetric measurements in hand for each of our sources it becomes interesting to investigate the spectral energy distributions (SEDs) of the LAEs to try and recover the properties (e.g. stellar mass, age, SFR, and dust content) of the underlying stellar populations in a way that does not rely on as many problematic assumptions as, for example, the SFR estimated from the rest-frame UV continuum flux that we calculate in Section 3.1 above. We compare our photometry for these sources against modified stellar population synthesis models. More details can be found in Wuyts et al. (2010), we only summarize the main procedure here. We use the revised templates of Bruzual and Charlot (CB07, based on Bruzual & Charlot (2003)) with solar metallicity, a Chabrier initial mass function (Chabrier 2003) and Calzetti (2000) dust extinction law. We investigate a range of exponentially declining star formation histories of the form $SFR(t) \sim \exp(t/\tau)$, with $e-$folding times τ =0.01, 0.05, 0.1, 0.2, 0.5, 1, 2 and 5 Gyr, as well as single bursts (SSP) and continuous star formation models (CSF). An updated version of the code *Hyperz* (Bolzonella 2000) is used to obtain the best-fit SED at the fixed spectroscopic redshift of the source via a maximum likelihood procedure.

The best-fit SED for SGAS J091541+382655 is shown in Figure 7 and corresponds to a dust-free single burst with an age of 1.4 Myr. It is important to supplement the best-fit stellar population parameters with confidence intervals allowed by the photometric uncertainties. We create 1000 fake realizations of the observed SED by perturbing each broadband magnitude measurement in a manner consistent with its errorbars. This set of fake SEDs is fit in exactly the same manner as described above for the observed SED; bad fits with $\chi^2 > 3$ are excluded. This procedure results in a very young (age ≤ 5 Myr) and dust-free ($E(B-V) \leq 0.01$) stellar population. Though we can place constraints on the age of the observed stellar population, are data are not sufficient for the SED fits to simultaneously constrain the star formation history, and consequently the current star formation rate, for this galaxy. After correcting for a lensing magnification factor of $\gtrsim 10$, we find a Chabrier stellar mass of $\mathrm{M}_{stars} \leq 7.9^{+3.7}_{-2.5} \times 10^7\ \mathrm{M}_\odot h_{0.7}^{-1}$.

SGAS J134331+415455 is detected in only 2 bands, which is insufficient to produce a robust best-fit stellar population. Instead, we compare the photometry to single burst, dust-free CB07 models of different ages to obtain some constraints on the age and stellar mass. The results are shown in Figure 8. The age of the observed stellar population lies in the range between 100 Myr and 400 Myr, which makes SGAS J134331+415455 significantly older than the very young stellar population seen in SGAS J091541+382655. After correcting for a lensing magnification factor of 12, we constrain the corresponding stellar masses to be within the range 2×10^8 $\mathrm{M}_\odot h_{0.7}^{-1} < \mathrm{M}_{stars} < 6 \times 10^9\ \mathrm{M}_\odot h_{0.7}^{-1}$. All of our photometric data for both of these sources sample light blueward of the 4000Å break in the source frame so that the stellar population parameters obtained from the SED fitting procedures correspond to the most recent episode of star formation in each LAE; we have no power to constrain stellar mass that may be present in an underlying population of older stars.

In addition to SED modeling of the photometry of both LAEs, we also examine the modest continuum signal that is detected for SGAS J091541+382655. Cross correlation of our GMOS spectrum for this source over a wavelength range of 1230-1350Å (source frame) against the composite LBG spectrum from Shapley et al. (2003) results in a peak at $z \sim 5.2$, in agreement with the redshift measured from the Lyman-α emission. We explicitly exclude the Lyman-α emission portion of the spectrum in this analysis so that the cross-correlation signal that we detect is entirely due to low-significance continuum features redward of Lyman-α. The composite LBG from Shapley et al. (2003) is plotted with our GMOS spectra

for both targets in Figures 2 and 3, and visual comparison of the continuum against the LBG composite spectrum suggests the presence of several strong UV metal absorption lines that are observed in well-studied LBGs at lower redshifts (e.g. Pettini et al. 2000). The features are at too low a significance in our data to claim a robust detection of individual absorption lines, but the cross correlation signal alone is encouraging given our low resolution spectra and limited integration time. Both of the sources presented here are excellent candidates for a more aggressive spectroscopic followup effort to explore the gas properties and stellar metallicity in representative low-mass starforming galaxies at $z \sim 5$.

4. SUMMARY AND CONCLUSIONS

We have identified two lensed Lyman-α emitting galaxies at $z \sim 5$ near the cores of strong lensing selected galaxy clusters. These sources are among the brightest galaxies identified at such high redshift, but their intrinsic luminosities are much lower than the observed flux due to magnification by the gravitational potential of foreground galaxy clusters. We use the available data to investigate the underlying stellar populations for these galaxies and find that the light – continuum and line emission – for SGAS 091541+382655 likely originates from a population of young stars with low dust content. Both sources are in the process of undergoing active star formation. Our analysis of these two LAEs corroborates our current understanding of the nature of Lyman-α emitting galaxies at high redshift, and the large magnification of these sources due to gravitational lensing makes them excellent candidates for studying the individual properties of galaxies on the faint end of the $L_{Ly-\alpha}$ and L_{UV} luminosity functions at $z \sim 5$. We encourage efforts to followup these sources aggressively on 8-10m class telescopes in order to better study the properties of the underlying stellar populations via continuum light. These sources are also excellent targets for space-based observations, both with current *HST* instruments and with *JWST* in the future.

We thank the anonymous referee for exceptionally thoughtful and helpful comments which helped to significantly improve the quality of this paper. MBB acknowledges the support of the Sigma Xi Scientific Research Society in the form of a grant in-aid of research. We also wish to thank the Gemini North observing and support staff for their efforts in taking data that contributed to this paper. The authors wish to recognize and acknowledge the very significant cultural role and reverence that the summit of Mauna Kea has always had within the indigenous Hawaiian community. We are most fortunate to have the opportunity to conduct observations from this mountain.

REFERENCES

Ajiki, M. et al 2003, AJ, 126, 2091A
Ajiki, M. et al 2004, PASJ, 56, 597A
Allam, S. S., Tucker, D. L.. Lin, H., Diehl, H. T., Annis, J., Buckley-Greer, E. J., and Frieman, J. A. 2007 ApJ, 662, L51
Bolzonella, M., Miralles, J.-M., and Pelló, R. 2000, A&A, 363, 476
Bond, N. A., Gawiser, E., Gronwall, C., Ciardullo, R., Altmann, M., Schawinski, K. 2009, ApJ, 705, 639B
Bond, N. A., Feldmeier, J. J., Matković, A., Gronwall, C., Ciardullo, R., Gawiser, E., 2010 , ApJ, 716, 200B
Bouwens, R. J., Illingworth, G. D.,Franx, M. and Ford, H. 2007 ApJ, 670, 928B
Bruzual, G. & Charlot, S. 2003, MNRAS, 344, 1000B
Calzetti, D., Armus, L., Bohlin, R. C., Kinney, A. L., Koornneef, J., and Storchi-Bergmann, T. 2000, ApJ, 533, 68
Chabrier, G. 2003 PASP, 115, 763c
Chary, R.-R., Stern, D., and Eisenhardt, P. 2005, ApJ, 635L, 5C
Cowie, L. L. & Hu, E. M. 1998, AJ, 115, 1319
Dawson, S., Rhoads, J. E., Malhotra, S., Stern, D., Wang, J., Dey, A., Spinrad, H., and Jannuzi, B. T. 2007, ApJ, 671, 1227D
Diehl, H. T. et al 2009, ApJ, 707, 686D
Dow-Hygelund, C. C. et al 2007, ApJ, 660, 47D
Finkelstein, S. L.; Rhoads, J. E., Malhotra, S., Grogin, N., and Wang, J. 2008, ApJ, 678, 655F
Finkelstein, S. L., Papovich, C., Giavalisco, M., Redd, N. A., Ferguson, H. C., Koekemoer, A. M.; and Dickinson, M. 2009, arXiv:0912.1338
Finkelstein, S. L., Papovich, C., Rudnick, G., Egami, E., Le Floc'h, E., Rieke, M. J., Rigby, J. R., and Willmer, C. N. A. 2009, ApJ, 700, 376
Finkelstein, S. L., Rhoads, J. E., Malhotra, S., and Grogin, N. 2009, ApJ, 691, 465F
Gawiser, E. et al 2006, ApJ, 642L, 13G
Gawiser, E. et al 2007, ApJ, 671, 278G
Giavalisco, M. AARA&A, 2002, 40, 579
Gilbank, D. G., Yee, H. K. C., Ellingson, E., Hicks, A. K., Gladders, M. D., Barrientos, L. F., and Keeney, B. 2008, ApJ, 677L, 89G
Gladders, M. D. & Yee, H. K. C. 2000, AJ, 120, 2148G
Glazebrook, K. & Bland-Hawthorn, J. 2001, PASP, 113, 197G
Gronwall, C., et al. 2007, ApJ, 667, 79G
Hennawi, J. F. et al. 2008, AJ, 135, 664H
Hook, I., Jørgensen, I., Allington-Smith, J. R., Davies, R. L., Metcalfe, N., Murowinski, R. G., and Crampton, D. 2004, PASP, 116, 425
Hu, E. M., Cowie, L. L., Capak, P., McMahon, R. G., Hayashino, T., and Komiyama, Y. 2004, AJ, 127, 563H
Jullo, E., Kneib, J.-P., Limousin, M., Elíasdóttir, Á., Marshall, P .J., and Verdugo, T. 2007, NJPh, 9, 447J
Kennicutt Jr., R. C. 1998, ARA&A, 36, 189K
Koester, B. P., Gladders, M. D., Hennawi, J. F., Sharon, K., Wuyts, E., Rigby, J. R., Bayliss, M. B., and Dahle, H. 2009, arXiv:1003.0030
Kurk, J. D., Cimatti, A., di Serego Alighieri, S., Vernet, J., Daddi, E., Ferrara, A., and Ciardi, B. 2004, A&A, 422L, 13K
Lai, K., Huang, J., Fazio, G., Cowie, L. L., Hu, E. M., and Kakazu, Y. 2007, ApJ, 655, 704L
Lowenthal, J. D. et al 1997, ApJ, 481, 673L
Murayama, T. et al 2007, ApJS, 172, 523M
McLure, R. J. and Cirasuolo, M. and Dunlop, J. S. and Foucaud, S. and Almaini, O. 2009, MNRAS, 395, 2196
Nilsson, K. K., Tapken, C., Møller, P., Freudling, W., Fynbo, J. P. U., Meisenheimer, K., Laursen, P., and Östlin, G. 2009, A&A, 498, 13N
Ouchi, M. et al. 2008, ApJS, 176, 301O
Peng, C. Y., Ho, L. C., Impey, C. D., Rix, H.-W. 2002, AJ, 124, 266
Pettini, M., Steidel, C. C., Adelberger, K. L., Dickinson, M., and Giavalisco, M. 2000, ApJ, 528, 96P
Pirzkal, N., Malhotra, S., Rhoads, J. E., Xu, C. 2007, ApJ, 667, 49P
Quider, A. M., Shapley, A. E., Pettini, M., Steidel, C. C., Stark, D. P. 2010, MNRAS, 402, 1467
Rauch, M. ARA&A, 1998, 36, 267
Riediger, R., Petitjean, P., and Mucket, J. P. 1998, A&A, 329, 30R
Rhoads, J. E., Malhotra, S., Dey, A., Stern, D., Spinrad, and Jannuzi, B. T. 2000, ApJ, 545L, 85R
Rhoads, J. E. et al 2003, AJ, 125, 1006R
Sawicki, M. et al 2008, ApJ, 687, 884S

Shapley, A., Steidel, C., Pettini, M., and Adelberger, K. L. 2003, ApJ, 588, 65
Shimasaku, K. et al. 2006, PASJ, 58, 313S
Shioya, Y. et al 2009, ApJ, 696, 546S
Siana, B. et al. 2009, ApJ, 698, 1273
Smail, I. et al. 2007, ApJ, 654, L33
Steidel, C. C. & Sargent, W. L. W. 1987, ApJ, 313, 171S
Steidel, C. C., Giavalisco, M., Dickinson, M., and Adelberger, K. L. 1996, AJ, 112, 352S
Steidel, C. C., Giavalisco, M., Pettini, M., Dickinson, M., and Adelberger, K. L. 1996, ApJ, 462L, 17S
Taniguchi, Y. et al 2009, ApJ, 701, 915T
Tapken, C., Appenzeller, I., Noll, S., Richling, S., Heidt, J., Meinköhn, E., and Mehlert, D. 2007, A&A, 467, 63T
Venemans, B. P. et al 2005, A&A, 431, 793V
Wen Z., et al. 2009, Research in Astron. Astrophys., 9, 5
Wuyts, E. et al. 2010, arXiv:1005.2621
Yabe, K., Ohta, K., Iwata, I., Sawicki, M., Tamura, N., Akiyama, M., and Aoki, K., 2009, ApJ, 693, 507Y
Yamada, S. F. et al 2005, PASJ, 57, 881Y
York, Donald G. et al 2000, AJ, 120, 1579